

A Deep *Chandra* View of a Candidate Parsec-Scale Jet from the Galactic Center Super-massive Black Hole

Zhenlin Zhu^{1,2}, Zhiyuan Li^{1,2}, Mark R. Morris³, Shuo Zhang⁴, Siming Liu⁵

¹ *School of Astronomy and Space Science, Nanjing University, Nanjing 210023, China*

² *Key Laboratory of Modern Astronomy and Astrophysics (Nanjing University), Ministry of Education, Nanjing 210023, China*

³ *Department of Physics and Astronomy, University of California, Los Angeles, CA 90095, USA*

⁴ *MIT Kavli Institute for Astrophysics and Space Research, Cambridge, MA 02139, USA*

⁵ *Purple Mountain Observatory, Chinese Academy of Science, Nanjing 210034, China*

zhuzl@smail.nju.edu.cn; lizy@nju.edu.cn

ABSTRACT

We have investigated the linear X-ray filament, G359.944-0.052, previously identified as a likely X-ray counterpart of a parsec-scale jet from the Galactic Center super-massive black hole (SMBH), Sagittarius A* (Sgr A*), using a total of ~ 5.6 Ms ultra-deep *Chandra* observations taken from September 1999 to July 2017. This unprecedented dataset enables us to examine flux and spectral variations that might be related to intrinsic properties of the weakly accreting SMBH. We find no flux or spectral variation in G359.944-0.052 after the G2 periapsis passage around early 2014, however, a moderate flux increase of $\sim 2\sigma$ significance might be associated with the periapsis passage of G1 in early 2001. The filament exhibits an unusually hard spectrum (photon-index $\lesssim 1$) in its portion closest to Sgr A* (i.e., near-side) and a significant spectral softening in the more distant portion, which can be interpreted as synchrotron cooling of the relativistic electrons moving along the jet path. In particular, the hard spectrum of the near-side suggests a piling up of quasi-monoenergetic electrons caused by rapid radiative cooling. The spectral and temporal properties of G359.944-0.052 strengthen the case of it being the X-ray counterpart of a jet launched by Sgr A*.

Subject headings: black hole physics – Galaxy: center – ISM: jets and outflows – radiation mechanisms: non-thermal – X-rays: individual (G359.944-0.052)

1. Introduction

Accretion onto a super-massive black hole (SMBH) can produce highly collimated, magnetized outflows of relativistic particles, i.e., jets. While the launching mechanism and composition of jets

are still not well understood, it is generally believed that jets can mediate the transport of an enormous amount of energy from the *central engine* to much greater physical scales, thus playing an important role in regulating the co-evolution of the SMBH and its environment (Meier 2012). As such, jets often manifest themselves as elongated features across a broad range of wavelengths, especially in the radio and X-ray bands where synchrotron and/or inverse Compton radiation from relativistic electrons are predominant. Spatially-resolved studies of such features have greatly facilitated our general understanding of jet energetics and kinematics.

Rather ironically, our knowledge about jets emanating from the closest SMBH, the one located in the Galactic center (GC) and best known as Sgr A* (Melia & Falcke 2001), remains elusive. On the one hand, numerous theoretical studies have demonstrated that the centimeter-to-millimeter emission from Sgr A* can well be interpreted as synchrotron radiation from a relativistic jet (e.g., Falcke et al. 1993; Falcke & Markoff 2000; Markoff et al. 2001; Yuan et al. 2002), which is likely symbiotic with a radiatively inefficient, advection-dominated accretion flow (Yuan & Narayan 2014). On the other hand, despite the continuing effort, observational searches for the putative jet, on sub-pc to kpc scales and over radio to γ -ray wavelengths, remain inconclusive (for an overview of the proposed jet candidates, see Li, Morris & Baganoff 2013; hereafter LMB13; see also Shahzamanian et al. 2015; Yusef-Zadeh et al. 2016).

Among the proposed jet manifestations, a narrow linear X-ray feature named G359.944-0.052 (hereafter G359.944 for brevity), originally identified by Munro et al. (2008) with *Chandra* observations and further studied by LMB13, is of special interest for several reasons. First, this feature traces the putative jet on a sub-pc scale, thus it can potentially help constrain any jet-driven feedback in the close vicinity of Sgr A*, as well as reveal short-term variations in the accretion process. Second, this feature is detected in X-rays and its power-law-shaped spectrum was found to be consistent with synchrotron emission. Due to the strongly magnetized environment of the GC, the synchrotron cooling timescale, on the order of ~ 1 yr (see discussion in Section 6), requires continuous energy input, which was suggested to originate from the putative jet dissipating its internal energy upon collision with one of the gas streamers constituting the so-called mini-spiral (Figure 1), first discovered by Lo & Claussen (1983) and Ekers et al. (1983) with the Very Large Array (VLA). Third, and perhaps physically most attractive, the inferred spatial orientation of G359.944 (hence that of the underlying jet) is aligned with the angular momentum of the Galactic disk. This alignment is what one might expect if: 1) the jet orientation is dictated by the SMBH’s spin axis, and 2) if the SMBH’s angular momentum has resulted from the accretion of stars and gas that had an average angular momentum reflecting that of the Galaxy. This special geometry, if true, is highly instructive for modeling the process of accretion onto Sgr A*. Indeed, recent studies combining numerical models and millimeter data seem to agree on a high inclination angle (with respect to our line-of-sight) of the spin axis (e.g., Vincent et al. 2015; Broderick et al. 2016), lending support to the inferred jet path.

The case for a jet can be reinforced if a relation between the variability of G359.944 and intrinsic variability of Sgr A* could be established. It has long been known that Sgr A* exhibits strong

variability in its broadband radiation, a phenomenon commonly dubbed *flares* (Baganoff et al. 2001; Genzel et al. 2003; Ghez et al. 2004). In particular, the X-ray flares of Sgr A* can reach peak fluxes ~ 10 – 100 times the quiescent level on a timescale of minutes (e.g., Baganoff et al. 2001; Porquet et al. 2003; Nowak et al. 2012; Zhang et al. 2017), strongly suggesting that they arise from merely a few gravitational radii from Sgr A*. At present, there is no consensus on the physical origin of the flares, but it is reasonable to associate flares with fluctuations or instabilities in the magnetized accretion flow (e.g., Chan et al. 2015; Ball et al. 2016; Li et al. 2017; Yuan et al. 2018). For this reason, when the G2 object, a hypothetical dusty cloud (with or without a central star; Gillessen et al. 2012; Witzel et al. 2014), was discovered to be moving on a highly eccentric orbit ($e \approx 0.98$) and approaching periapsis around early 2014, there was heated anticipation that it might boost accretion onto Sgr A* and trigger strong radiation. Indeed, an increase in the frequency of bright X-ray flares a few months after the periapsis passage of G2 was suggested by Ponti et al. (2015) (see also Mossoux & Grosso 2017). On the other hand, no significant excess was seen at other wavelengths after the periapsis passage (For radio, see Park et al. 2015; Tsuboi et al. 2015; For infrared, see Witzel et al. 2018; For γ -rays, see Ahnen et al. 2017).

The jet power is generally thought to be correlated with the accretion rate (Yuan & Narayan 2014). In this regard, a parsec-scale jet may provide additional insight to the accretion process that is possibly affected by tidal interaction between Sgr A* and G2 or similar objects (e.g., G1; Witzel et al. 2017). In this work, we aim to revisit the case of G359.944 being the X-ray counterpart of the Sgr A* jet, taking advantage of the extensive *Chandra* observations of the GC in the past two decades. Our focus is devoted to probing flux and spectral variations in G359.944, and to further constraining the X-ray radiation mechanism and underlying jet properties.

We describe the *Chandra* data in Section 2. The spatial properties of G359.944 are reviewed in Section 3. Analysis of the flux variability is presented in Section 4. In Section 5, we examine the spatially-resolved and time-dependent spectra of G359.944. Implications for the radiation mechanism and jet properties are discussed in Section 6, followed by a summary in Section 7. We adopt a distance of 8 kpc for the GC (Ghez et al. 2008; Gillessen et al. 2009).

2. Data Preparation

The inner few parsecs centered on Sgr A* have been frequently visited by the *Chandra X-ray Observatory* since launch, chiefly with its Advanced CCD Imaging Spectrometer (ACIS). In this work, we utilize 47 ACIS-I observations taken between September 1999 and March 2011, 38 ACIS-S observations with the High Energy Transmission Grating (HETG) taken between February and October 2012, and 39 ACIS-S non-grating observations taken between May 2013 and July 2017.

All these observations had their aimpoint placed within $1'$ from Sgr A*¹, thus ensuring an optimal point-spread function for narrow features like G359.944. The ACIS-I data are essentially the same as used in LMB13. The ACIS-S non-grating (hereafter referred to as ACIS-S) observations, while taken in a 1/8 subarray mode, have a sufficiently large field-of-view to cover G359.944 and serve to substantially extend the temporal baseline, especially around the periapsis passage of G2.

Our data reduction procedure is detailed in Zhu, Li & Morris (2018), in which we have combined the ACIS-I and ACIS-S/HETG (hereafter simply referred to as HETG) observations to obtain the deepest ever X-ray source catalog of the GC. The main steps are briefly described below. We uniformly reprocessed the level 1 event files with CIAO v4.9 and the corresponding calibration files, following the standard pipeline². The light curve of each ObsID was examined, and when necessary, was filtered to remove time intervals contaminated by significant particle flares. This resulted in a total cleaned exposure of 1.42 Ms from ACIS-I, 2.83 Ms from HETG and 1.33 Ms from ACIS-S. The three datasets have comparable sensitivities³, and when combined, they roughly double the signal-to-noise ratio (S/N) as achieved in LMB13 for G359.944. It is noteworthy that two ACIS-I observations, ObsID 5360 and 6639, suffer from relatively high particle background throughout their short exposures, thus they were excluded from the following analysis. In total, 122 observations spanning 5.58 Ms are included in this work. More specific information on the datasets are listed in Table 1. After the cleaned level 2 event file was created for each ObsID, we produced a merged event file by reprojecting all events to a common tangential point, i.e., the position of Sgr A* ([RA, DEC]=[17:45:40.038, -29:00:28.07] at epoch J2000). We also generated exposure maps in the 2–8 keV band for each observation, assuming an incident spectrum of an absorbed bremsstrahlung. The lower energy cutoff is justified by the large foreground absorption column density $N_{\text{H}} \sim 10^{23} \text{ cm}^{-2}$ (e.g., Zhu et al. 2018). The individual exposure maps of the same instrument (i.e., ACIS-I, HETG or ACIS-S) were then reprojected to form a combined exposure map.

In addition, we have acquired ancillary VLA and *NuSTAR* images, chiefly to obtain constraints on the flux of G359.944 at radio frequencies and in hard X-rays. Details of the VLA images can be found in Zhao et al. (2009; see also LMB13). We analyzed the *NuSTAR* data obtained in 2012 (obsID: 30002001001, 30002001003 and 30002001004), an epoch with no X-ray transient contaminating the inner few parsecs around Sgr A* (S. Zhang et al. in preparation). Using the selected dataset, we extracted the source spectrum and the background spectrum from an annular region that can properly represent the PSF contamination from the bright pulsar wind nebula (PWN) candidate G359.95-0.04 (Wang et al. 2006) at the location of G359.944. We found that

¹Two ACIS-I observations (ObsID 14941 and 14942) taken in 2013 also satisfy this criterion. These two ObsIDs are not included here, since we wish to have a clear temporal division between the three datasets.

²<http://cxc.harvard.edu/ciao>

³With the HETG inserted, about half of the incident X-rays are dispersed, while the remaining X-rays continue to the detector directly and form the “zeroth-order” image.

G359.944 is detected at only 1σ confidence level in 3–79 keV, and lower than 1σ in the 3–10, 10–20 and 20–40 keV energy bands. In 10–40 keV, the 3σ flux upper limit is 1.5×10^{-13} erg cm $^{-2}$ s $^{-1}$, assuming a representative photon-index of 1.0 (see Section 5).

3. Spatial Properties of G359.944-0.052

A 2–8 keV counts image combining the 122 *Chandra* observations is shown in Figure 1, highlighting the X-ray filament G359.944 and the X-ray-bright Sgr A complex. Also shown are VLA 8.4 GHz intensity contours tracing the ionized gas streamers of the mini-spiral (Zhao et al. 2009). The highly linear morphology of G359.944 and its almost perfect alignment with Galactic latitude can be clearly seen in the figure. The fact that the extrapolation of the straight line defined by G359.944 points back to Sgr A*, had led Muno et al. (2008) and LMB13 to associate G359.944 with the putative jet. LMB13 further identified a shock front on the Eastern Arm of the mini-spiral (at an offset of $[\Delta\alpha, \Delta\delta] = [12''.8, 7''.7]$ from Sgr A*, as marked by the white ‘X’ in Figure 1), which they interpreted as the site where the jet penetrates through and dissipates energy to the ionized gas. Consequently, G359.944 can be understood as the synchrotron radiation from shock-induced relativistic electrons cooling in a finite post-shock region downstream from the shock along the jet path.

We revisit the above qualitative picture with the updated X-ray data. For a quantitative analysis, we follow LMB13 to adopt the hypothetical jet path as pointing away from Sgr A* at a position angle of $124^\circ 5$. Visual examination indicates that this remains an optimal definition for the linear filament in the current X-ray image of significantly enhanced counting statistics. LMB13 suggested that the filament is unresolved along its short-axis. We update this view by comparing the intensity distribution of G359.944 along its short-axis with that of nearby point sources. The derived FWHM is $\sim 1''.1$ for the former and $\sim 0''.8$ for the latter, suggesting that the filament is marginally resolved along its short-axis, having a linear width of ~ 0.04 pc at the assumed distance of 8 kpc. We emphasize that the average PSF should have a negligible variation along G359.944.

The exposure map corrected 2–8 keV intensity profile along the long-axis of G359.944 is shown in the upper row of Figure 2, with the three panels displaying the ACIS-I, HETG and ACIS-S data in order. To account for the local background, we have adopted an adjacent box running in parallel with the filament. It is clear that the intensity profile looks similar among the three datasets, indicating no drastic changes in the morphology of G359.944 over the past two decades. According to the presumed physical picture, X-ray emission can be induced immediately downstream the shock front (taken in Figure 2 as the zero point of the intensity profile). However, as already noted in LMB13 and illustrated in Figure 1, the presence of relatively strong and non-uniform diffuse emission around the shock front hampers an accurate determination of the local background thereof. To test this possibility, we subtract no background for the first bin ($\lesssim 3''$) of the intensity profile, which thus represents a firm upper limit at the position. It turns out that this upper limit is compatible with the X-ray filament starting from the shock front. In practice, however, we define

the filament as starting at $3''$ and ending at $10''.5$ (i.e., an apparent length of $7''.5$, corresponding to a physical length of ~ 0.3 pc), beyond which point the filament again loses its trace into the diffuse background. The otherwise smooth intensity profile exhibits a “knot” at $\sim 5''$, the nature of which is further examined in Section 4. For the three individual datasets (ACIS-I, HETG, ACIS-S) and the combined dataset, we find 440/382/504/1326 net counts out of a total (source plus background) of 1049/935/1469/3453 counts, giving a 13.6/12.5/13.1/22.6 σ significance to G359.944.

In the lower row of Figure 2, we present the hardness ratio (HR) profile, where $\text{HR} \equiv (I_{4-8 \text{ keV}} - I_{2-4 \text{ keV}})/(I_{4-8 \text{ keV}} + I_{2-4 \text{ keV}})$, and I denotes the intensity of a given band. The three datasets again agree with each other, showing an overall trend of softening toward the far-side of the filament (a flat HR profile is rejected at 78%/61%/92% confidence level for the ACIS-I/HETG/ACIS-S profiles). As suggested by LMB13, this trend can be understood as synchrotron cooling of the relativistic electrons moving along the jet path. We can estimate a synchrotron cooling timescale $\tau_{\text{syn}} \sim 0.3(\gamma_e m_e c^2 / 50 \text{ TeV})^{-1} (B/1 \text{ mG})^{-2} \text{ yr}$ (see Section 6 for details), which is comparable to the light crossing time of ~ 1.3 yr. In the meantime, the consistency of the HR profile among the three datasets suggests a stable supply of relativistic electrons at least over the past two decades. This, however, does not preclude flux and spectral variability on smaller timescales, which will be examined in the following sections.

4. Flux Variation of G359.944-0.052

We first probe flux variation in G359.944 by examining the mean 2–8 keV photon flux in all 122 observations (individual values are listed in Table A1). The source and background regions are outlined by the two rectangles in the insert of Figure 1. We utilize the CIAO tool *aprates*, which applies a Bayesian approach for Poisson statistics in the low-count regime, to compute the photon flux and bounds for each observation, corrected for the local effective exposure. For those observations with limited net counts, we derive the 3σ upper limit. The resultant long-term light curve, as shown in Figure 3, exhibits no significant inter-observation variability. This is supported by the *normalized excess variance* (Nandra et al. 1997; Turner et al. 1999), $\sigma_{\text{rms}}^2 \equiv \sum_{i=1}^N [(f_i - \bar{f})^2 - \sigma_{f,i}^2] / (N\bar{f}^2) \approx -0.049$, with 68% error equaling 0.033, which indicates that the apparent deviations from the mean photon flux, $\bar{f} \approx 1.5 \times 10^{-6} \text{ ph cm}^{-2} \text{ s}^{-1}$, arise predominantly from statistical fluctuations.

Since the filament has a length of more than one light year, we do not expect to detect intra-observation variability across the whole filament. On the other hand, short-term variability might be seen in the “knot”, which is essentially unresolved in the X-ray image of Figure 1. Therefore, we search for its variability, employing the CIAO tool *glvary* on each of the 122 observations. This tool uses the Gregory-Loredo variability test algorithm (Gregory & Loredo 1992) on the unbinned X-ray data. We have run the *dither_region* tool to produce a normalized effective area file, to be fed to *glvary*, which accounts for the dead time due to bad pixels or chip gaps. This step ensures that any measured time variation is intrinsic and not caused by the telescope dithering. The output

of *glvary* assigns a variability index that takes values from 0 to 10, with values ≥ 6 indicating a definitely variable source. Probable intra-observation variability is only found in one out of the 122 observations, as indicated by its variability index of 6. This strongly suggests that the knot maintains a rather stable flux over the past two decades, thus it is unlikely a stellar object.

5. Spectral Properties of G359.944-0.052

We now turn to examine the spatially-resolved and time-dependent spectral properties of G359.944. The spectra are extracted from each ObsID using the CIAO tool *specextract*. For the whole filament, the source and background regions are again defined by the two rectangles in Figure 1. The tool also generates the ancillary response files (ARFs) and redistribution matrix files (RMFs), weighted over the source region. We then produce an average spectrum of ACIS-I, HETG or ACIS-S, by combining ObsIDs taken with the same instrument and weighting the ARFs and RMFs by the effective exposure. We note that although the instrumental response of *Chandra* has degraded over the years of its operation, the effective area of a given instrument above ~ 2 keV (i.e., the energy range of interest) has undergone no significant change, which justifies the analysis of the combined spectra. Throughout this section we report errors at 90% confidence level unless otherwise noted.

All fitted spectra are adaptively binned to achieve S/N better than 3 per bin over the range of 1–9 keV. As shown in Figure 4a, all three spectra appear featureless (i.e., consistent with non-thermal emission) and can be well-fitted with an absorbed power-law model, *tbabs*powerlaw* in XSPEC v12.9.1 (Wilms et al. 2000). It is reasonable to assume that the absorption column density toward the inner $30''$ around Sgr A* does not significantly vary on a timescale of two decades, thus we apply a joint fit to the three spectra, linking the column density but allowing the photon-index to vary. This yields $N_{\text{H}} = 17.6^{+5.1}_{-4.2} \times 10^{22} \text{ cm}^{-2}$, consistent with the typical value derived from X-ray point sources in this region (Zhu et al. 2018). The best-fit photon-index (Γ_1) is largest ($1.40^{+0.50}_{-0.50}$) in the ACIS-I spectrum and smallest ($0.62^{+0.58}_{-0.60}$) in the ACIS-S spectrum, suggesting the two values differ at 90% significance. In the meantime, a possible small increase in the unabsorbed 2–10 keV luminosity is found in the ACIS-S spectrum, by $\sim (30 \pm 20)\%$ as compared to the ACIS-I spectrum (Column 6 of Table 2). The observed spectrum might have been manipulated by foreground dust scattering, which results in spectral hardening due to an E^{-2} dependence in the scattering cross-section (Predehl & Schmitt 1995). We assess this effect under extreme case that the dust scattering is concentrated in a thin plane, obtaining a column density $N_{\text{H}} = 13.1^{+6.8}_{-4.8} \times 10^{22} \text{ cm}^{-2}$. The corresponding best-fit photon-indices (Γ_2 ; Column 8 of Table 2) become slightly larger as expected. However, even under this extreme case, it holds true that the ACIS-S spectrum is rather flat ($\Gamma_2 = 0.83^{+0.58}_{-0.61}$). Below we shall neglect the effect of dust scattering.

As evident in Figure 2, the filament exhibits gradual softening towards the far-side. To quantify this softening, we divide the source rectangle into two equal halves and extract a spectrum for each half (Figure 4b-d). We tie the absorption column densities of both halves to the best-fit value,

$N_{\text{H}} = 17.6 \times 10^{22} \text{ cm}^{-2}$, found for the whole filament. This is justified by the fact that K-band foreground extinction across this region varies by less than 10% (Schödel et al. 2010). We note that fixing the absorption column density effectively eliminates its degeneracy with the photon-index and thus artificially reduces the estimated uncertainty of the latter. However, it is the relative change in the photon-index, spatially or temporally, that we are most interested in here. The best-fit photon-indices, listed in rows 4 to 9 of Table 2 for the three instruments, are different between the near-half and the far-half at more than 95% confidence level. In particular, the near-half exhibits a very flat spectrum ($\Gamma_1 < 1$) in both HETG and ACIS-S. It is noteworthy that the knot does not dominate the flux of the near-half, nor does it show a distinct HR (Figure 2). The far-half, in contrast, shows a steep spectrum consistent with the softening trend seen in the HR profile. The unabsorbed 2–10 keV luminosity of the near-half is about 2 times that of the far-half.

As discussed in Section 4, the statistical uncertainty and the finite light-crossing time may smear any moderate intrinsic variability in G359.944. In order to reduce the statistical errors, we divide the 18 years of observations into several epochs, requiring at least 300 ks exposure and a minimum baseline of 2 yrs in each epoch. We also ensure that observations from different instruments are not brought into the same epoch. As summarized in Table 3, we eventually choose 6 epochs and group the ObsIDs assigned to each epoch to extract a combined spectrum for the whole filament. 5% of the total exposure from 23 observations are excluded. The fitted results of the combined spectra are shown in Figure 5. G359.944 reached the softest state ($\Gamma = 1.94_{-0.67}^{+0.64}$) in epoch 2002.2-2002.6, and became harder ($\Gamma = 0.08_{-1.23}^{+1.12}$) in epoch 2008.5-2010.5, at $\sim 95\%$ significance. To see whether this apparent difference can be attributed to pure statistical fluctuations about a constant power-law spectrum, we employ *multifake* in XSPEC to simulate 1000 spectra for each epoch, feeding the tool with the corresponding ARFs and RMFs and assuming a fixed photon-index of $\Gamma = 1.15$ and unabsorbed 2–10 keV luminosity $L_{2-10} = 2.0 \times 10^{32} \text{ erg s}^{-1}$, which represent the long-term mean of the observed spectra. The fake spectra are then fitted to derive the 90% percentile of the best-fit parameters, which are taken as the range of statistical fluctuations (the grey strips in Figure 5a). The results suggest that there is intrinsic variation in the photon-index of both epochs 2002.2-2002.6 and 2008.5-2010.5. The apparent variation in L_{2-10} , however, can be accounted for by statistical fluctuations. Furthermore, as illustrated in Figure 5b, there is no significant correlation between L_{2-10} and Γ , according to the Spearman’s rank correlation coefficient $r = 0.31$, with the p-value of 0.54 for random correlation.

6. Discussion

It was anticipated that the periapsis passage of G2, occurring at $T_0 \sim 2014.2$ (marked by a vertical dashed line in Figure 3; Witzel et al. 2017), might boost accretion onto Sgr A* due to its partial disruption under the strong tidal force of the SMBH. However, there seems to be no observational evidence for a dramatic change in the accretion rate, which is presumably manifested by Sgr A*’s broadband radiation, in particular, its quiescent X-ray flux within the *Bondi radius*

(Yuan & Wang 2016; Ahnen et al. 2017; Witzel et al. 2018). On the other hand, Ponti et al. (2015) and Mossoux & Grosso (2017) claimed evidence for an enhanced incidence rate of bright X-ray flares a few months after G2’s periapsis passage. We note that this time delay is comparable to the free-fall time at the periapsis distance of G2 (~ 200 AU; Witzel et al. 2017). If the passage of G2 also had an effect on the putative jet traced by G359.944, we would expect to probe the associated variations after a time delay of $\gtrsim 2$ yrs, given the distance of G359.944 from Sgr A*. Thanks to the high-cadence ACIS-S observations since 2013, such an effect can be readily probed. However, no significant flux variation can be seen when comparing the epochs 2013.5-2014.10 and 2015.5-2017.4 (blue and magenta points in Figure 3 and Figure 5b), assuming that the former epoch represents the normal state of the jet. We also examine the light curve near the periapsis passage of G1 at $T_0 \sim 2001.3$. G1 has similar observational properties with G2 in the near-infrared and shows signs of tidal expansion after periapsis passage (Witzel et al. 2017). Interestingly, at epoch 2002.2-2002.6, G359.944 exhibits ~ 2 times flux increase ($\sim 2\sigma$ significance) as compared to the mean flux before the G1 passage. We caution that a real physical connection is highly uncertain due to the sparse *Chandra* observations before and after this epoch.

In the proposed jet scenario, relativistic electrons, accelerated at the shock front and streaming down the jet path, are responsible for the observed non-thermal X-ray emission from G359.944. LMB13 showed that inverse Compton radiation can be ruled out, due to the lack of sufficient seed photons at lower frequencies (e.g., constrained by the upper limits in the radio band as illustrated in Figure 6), which left synchrotron as the most viable radiation mechanism. Here, we argue that the observed flat spectra, in particular those from the near-half, place strong constraints even on the synchrotron scenario.

According to the standard diffusive shock acceleration (DSA) theory (e.g., Drury 1983), post-shock electrons acquire a power-law energy distribution, which can be expressed as: $N(\gamma_e) = K\gamma_e^{-p}$, where γ_e is the Lorentz factor and K the normalization factor. The slope p is determined by the shock compression ratio χ as $p = (\chi + 2)/(\chi - 1)$, while χ itself can be written as $\chi = (\gamma + 1)/(\gamma - 1 + M^{-2})$ via the adiabatic index γ and Mach number M . Therefore, in the case of a strong shock in a non-relativistic plasma, $\gamma = 5/3$ and $M \rightarrow \infty$, we obtain the canonical value of $p = 2$, and the corresponding photon-index $\Gamma = (p + 1)/2 = 1.5$. The broadband spectral energy distribution (SED)⁴ of such a case is shown as the solid line in Figure 6. We have assumed an empirical magnetic field strength $B \approx 1$ mG at the central parsec (Plante et al. 1995; Eatough et al. 2013), and the minimum/maximum Lorentz factors $\gamma_{e,\min} = 1$ and $\gamma_{e,\max} = 10^8$. Evidently, this canonical synchrotron cannot account for the flatness of the near-half spectra obtained with ACIS-I, HETG and ACIS-S, with $\Gamma = 0.92_{-0.53}^{+0.53}$, $0.20_{-0.68}^{+0.66}$ and $-0.10_{-0.66}^{+0.63}$, respectively (see solid lines in Figure 6). If we further take into account the fact that the strong shock is propagating in the

⁴Model calculations and figure plotting are realized with *Naima* (Zabalza 2015), a Python package for computation of non-thermal radiation from relativistic particle populations, publicly available at <https://naima.readthedocs.io/en/latest/>

relativistic plasma of the jet, i.e., $\gamma = 4/3$, we can obtain a harder slope of $p = 1.5$ and $\Gamma = 1.25$. This latter value, however, still cannot account for the HETG and ACIS-S spectra.

The flat spectrum motivates us to consider synchrotron from monoenergetic electrons, i.e., represented by a δ -function distribution: $N(\gamma_e) = N_0\delta(\gamma_e - \gamma_{e,0})$ (Pacholczyk 1970). When $\gamma_{e,0} \rightarrow \infty$, the corresponding SED asymptotically approaches $EdN/dE \propto E^{0.3}$, that is, a photon-index $\Gamma = 0.7$, which in principle is the flattest possible synchrotron spectrum. This value barely falls within the uncertainties of the photon-indices of the HETG and ACIS-S near-half spectra (Table 2). In Figure 6, we plot the synchrotron spectrum of monoenergetic electrons with an energy of $\gamma_{e,0}m_e c^2 = 50$ TeV (dashed curve) and $\gamma_{e,0}m_e c^2 = 5$ TeV (dotted curve), the former approximately matching the observed near-half spectra and the latter consistent with the far-half spectra. We note that these SEDs are fully compatible with the non-detections in radio as well as the $3\text{-}\sigma$ upper limit on the 10–40 keV flux as constrained by *NuSTAR*.

In reality, a population of quasi-monoenergetic electrons may be generated from rapid synchrotron cooling of an initial population having a power-law energy distribution (Rybicki & Lightman 1986):

$$N(\gamma_e)d\gamma_e = N_i(\gamma_{e,i})d\gamma_{e,i} \propto \gamma_{e,i}^{-p}d\gamma_{e,i}, \quad (1)$$

$$\frac{d\gamma_e}{dt} = -\frac{1}{m_e c^2} \frac{4}{3} \sigma_T c \beta_e^2 \frac{B^2}{8\pi} \gamma_e^2 \equiv -A\gamma_e^2, \quad (2)$$

where $p > 1$ is the initial power-law slope, σ_T is the Thomson scattering cross-section, $\beta_e \approx 1$ is the electron velocity relative to the speed of light (c). We have $A \approx 1.3 \times 10^{-15} (B/1 \text{ mG})^2 \text{ s}^{-1}$. From Equations (1) and (2), we can derive the time-dependent electron energy distribution:

$$N(\gamma_e) \propto \gamma_e^{-p} (1 - At\gamma_e)^{p-2}, \quad (3)$$

where t is the cooling time. For $1 < p < 2$, the electron energy distribution will evolve into a quasi- δ -function peaking at $\gamma_e = 1/(At)$ (Schlickeiser 1984). We can estimate the time needed for electrons cooling from the near-half (e.g., $\gamma_{e,n}m_e c^2 \approx 50$ TeV) to the far-half (e.g., $\gamma_{e,f}m_e c^2 \approx 5$ TeV) along the jet path: $\Delta t = 1/(A\gamma_{e,f}) - 1/(A\gamma_{e,n}) \approx 2.2(B/1 \text{ mG})^{-2} \text{ yr}$. This cooling time is compatible with the half-length of G359.944, ~ 0.15 pc, if the bulk motion of the electrons is relativistic as expected for a jet. We conclude that the above simple model is consistent with the physical picture proposed by LMB13: the putative jet drives a bow-shock in the Eastern Arm and generates ultra-relativistic electrons, which cool by synchrotron radiation and produce the observed X-ray filament downstream the shock along the jet path.

7. Summary

We have utilized ~ 5.6 Ms of *Chandra* observations spanning 18 years to study the X-ray properties of G359.944, a very promising candidate for a jet from Sgr A*. Our main results include:

- The periapsis passage of G2 in early 2014 does not seem to have caused significant variation in the X-ray spectrum of G359.944. On the other hand, a flux enhancement of $\sim 2\sigma$ significance, might be associated with the periapsis passage of G1 in early 2001.
- Unusually hard spectra are found in the near-half of G359.944, showing a photon-index as low as $-0.10_{-0.66}^{+0.63}$. The spectrum becomes softer and less luminous further down the putative jet path. Such properties can be best understood as rapid synchrotron cooling of the ultra-relativistic electrons.

We conclude that G359.944 remains a viable candidate for the long-sought jet from Sgr A*. A decisive test may come from imaging of the Event Horizon Telescope available in the near future (Psaltis et al. 2015). Regardless of the validity of G359.944 being the jet, its unusually flat spectrum is intriguing. Previous work has identified more than a dozen filamentary X-ray features within the inner parsecs of the GC (Muno et al. 2008; Lu et al. 2008; Johnson et al. 2009). Some of these filaments are identified as magnetic flux tubes (Zhang et al. 2014; Morris et al. 2014), while others might be PWN driven by a fast-moving pulsar (Wang et al. 2006; S. Zhang, et al. in prep.). It is noteworthy that all known Galactic PWNe show a power-law X-ray spectrum with photon-indices of 1.1-2.2 (Kargaltsev et al. 2017). Six out of the 17 X-ray filaments studied by Johnson et al. (2009) showed a flat spectrum with best-fit photon-index $\lesssim 1.0$ with large uncertainties due to the limited counting statistics. It will be an important step to revisit the spectral and temporal properties of these filaments using the updated *Chandra* data, which will facilitate a comparison with the case of G359.944 and help us understand the behavior of high-energy particles in the unique GC environment.

This work is supported by National Science Foundation of China under grant 11473010. We acknowledge the PIs of the *Chandra* programs, in particular Fred Baganoff, for acquiring the data that made this work possible. Z.Z. thanks Xiao Zhang for helpful discussions on the jet model.

REFERENCES

- Ahnen, M. L., Ansoldi, S., Antonelli, L. A., et al. 2017, *A&A*, 601, A33
- Baganoff, F. K., Bautz, M. W., Brandt, W. N., et al. 2001, *Nature*, 413, 45
- Ball, D., Özel, F., Psaltis, D., & Chan, C.-k. 2016, *ApJ*, 826, 77
- Broderick, A. E., Fish, V. L., Johnson, M. D., et al. 2016, *ApJ*, 820, 137
- Chan, C.-k., Psaltis, D., Özel, F., et al. 2015, *ApJ*, 812, 103
- Drury, L. O. 1983, *Reports on Progress in Physics*, 46, 973
- Eatough, R. P., Falcke, H., Karuppusamy, R., et al. 2013, *Nature*, 501, 391

- Ekers, R. D., van Gorkom, J. H., Schwarz, U. J., & Goss, W. M. 1983, *A&A*, 122, 143
- Falcke, H., Mannheim, K., & Biermann, P. L. 1993, *A&A*, 278, L1
- Falcke, H., & Markoff, S. 2000, *A&A*, 362, 113
- Gaensler, B. M., & Slane, P. O. 2006, *ARA&A*, 44, 17
- Genzel, R., Schödel, R., Ott, T., et al. 2003, *Nature*, 425, 934
- Ghez, A. M., Salim, S., Weinberg, N. N., et al. 2008, *ApJ*, 689, 1044
- Ghez, A. M., Wright, S. A., Matthews, K., et al. 2004, *ApJ*, 601, L159
- Gillessen, S., Eisenhauer, F., Trippe, S., et al. 2009, *ApJ*, 692, 1075
- Gillessen, S., Genzel, R., Fritz, T. K., et al. 2012, *Nature*, 481, 51
- Gregory, P. C., & Loredó, T. J. 1992, *ApJ*, 398, 146
- Johnson, S. P., Dong, H., & Wang, Q. D. 2009, *MNRAS*, 399, 1429
- Kargaltsev, O., Klingler, N., Chastain, S., & Pavlov, G. G. 2017, *Journal of Physics Conference Series*, 932, 012050
- Li, Y.-P., Yuan, F., & Wang, Q. D. 2017, *MNRAS*, 468, 2552
- Li, Z., Morris, M. R., & Baganoff, F. K. 2013, *ApJ*, 779, 154 (LMB13)
- Lo, K. Y., & Claussen, M. J. 1983, *Nature*, 306, 647
- Lu, F. J., Yuan, T. T., & Lou, Y.-Q. 2008, *ApJ*, 673, 915
- Markoff, S., Falcke, H., Yuan, F., & Biermann, P. L. 2001, *A&A*, 379, L13
- Meier, D. L. 2012, *Black Hole Astrophysics: The Engine Paradigm*, by David L. Meier. ISBN: 978-3-642-01935-7. Springer, Verlag Berlin Heidelberg, 2012,
- Melia, F., & Falcke, H. 2001, *ARA&A*, 39, 309
- Morris, M. R., Zhao, J.-H., & Goss, W. M. 2014, *The Galactic Center: Feeding and Feedback in a Normal Galactic Nucleus*, 303, 369
- Mossoux, E., & Grosso, N. 2017, *A&A*, 604, A85
- Muno, M. P., Baganoff, F. K., Brandt, W. N., Morris, M. R., & Starck, J.-L. 2008, *ApJ*, 673, 251
- Nandra, K., George, I. M., Mushotzky, R. F., Turner, T. J., & Yaqoob, T. 1997, *ApJ*, 476, 70
- Nowak, M. A., Neilsen, J., Markoff, S. B., et al. 2012, *ApJ*, 759, 95

- Pacholczyk, A. G. 1970, *Radio Astrophysics: Nonthermal Processes in Galactic and Extragalactic Sources*. Freeman & Co., San Francisco
- Park, J.-H., Trippe, S., Krichbaum, T. P., et al. 2015, *A&A*, 576, L16
- Plante, R. L., Lo, K. Y., & Crutcher, R. M. 1995, *ApJ*, 445, L113
- Ponti, G., De Marco, B., Morris, M. R., et al. 2015, *MNRAS*, 454, 1525
- Porquet, D., Predehl, P., Aschenbach, B., et al. 2003, *A&A*, 407, L17
- Predehl, P., & Schmitt, J. H. M. M. 1995, *A&A*, 293, 889
- Psaltis, D., Narayan, R., Fish, V. L., et al. 2015, *ApJ*, 798, 15
- Rybicki, G. B., & Lightman, A. P. 1986, *Radiative Processes in Astrophysics*, by George B. Rybicki, Alan P. Lightman, pp. 400. ISBN 0-471-82759-2. Wiley-VCH, June 1986., 400
- Schödel, R., Najarro, F., Muzic, K., & Eckart, A. 2010, *A&A*, 511, A18
- Schlickeiser, R. 1984, *A&A*, 136, 227
- Shahzamanian, B., Eckart, A., Valencia-S., M., et al. 2015, *A&A*, 576, A20
- Tsuboi, M., Asaki, Y., Kameya, O., et al. 2015, *ApJ*, 798, L6
- Turner, T. J., George, I. M., Nandra, K., & Turcan, D. 1999, *ApJ*, 524, 667
- Vincent, F. H., Yan, W., Straub, O., Zdziarski, A. A., & Abramowicz, M. A. 2015, *A&A*, 574, A48
- Wang, Q. D., Lu, F. J., & Gotthelf, E. V. 2006, *MNRAS*, 367, 937
- Wang, Q. D., Nowak, M. A., Markoff, S. B., et al. 2013, *Science*, 341, 981
- Wilms, J., Allen, A., & McCray, R. 2000, *ApJ*, 542, 914
- Witzel, G., Ghez, A. M., Morris, M. R., et al. 2014, *ApJ*, 796, L8
- Witzel, G., Martinez, G., Hora, J., et al. 2018, *ApJ*, 863, 15
- Witzel, G., Sitarski, B. N., Ghez, A. M., et al. 2017, *ApJ*, 847, 80
- Yuan, F., Markoff, S., & Falcke, H. 2002, *A&A*, 383, 854
- Yuan, F., & Narayan, R. 2014, *ARA&A*, 52, 529
- Yuan, Q., & Wang, Q. D. 2016, *MNRAS*, 456, 1438
- Yuan, Q., Wang, Q. D., Liu, S., & Wu, K. 2018, *MNRAS*, 473, 306

- Yusef-Zadeh, F., Wardle, M., Schödel, R., et al. 2016, *ApJ*, 819, 60
- Zabalza, V. 2015, 34th International Cosmic Ray Conference (ICRC2015), 34, 922
- Zhang, S., Baganoff, F. K., Ponti, G., et al. 2017, *ApJ*, 843, 96
- Zhang, S., Hailey, C. J., Baganoff, F. K., et al. 2014, *ApJ*, 784, 6
- Zhao, J.-H., Morris, M. R., Goss, W. M., & An, T. 2009, *ApJ*, 699, 186
- Zhu, Z., Li, Z., & Morris, M. R. 2018, *ApJS*, 235, 26

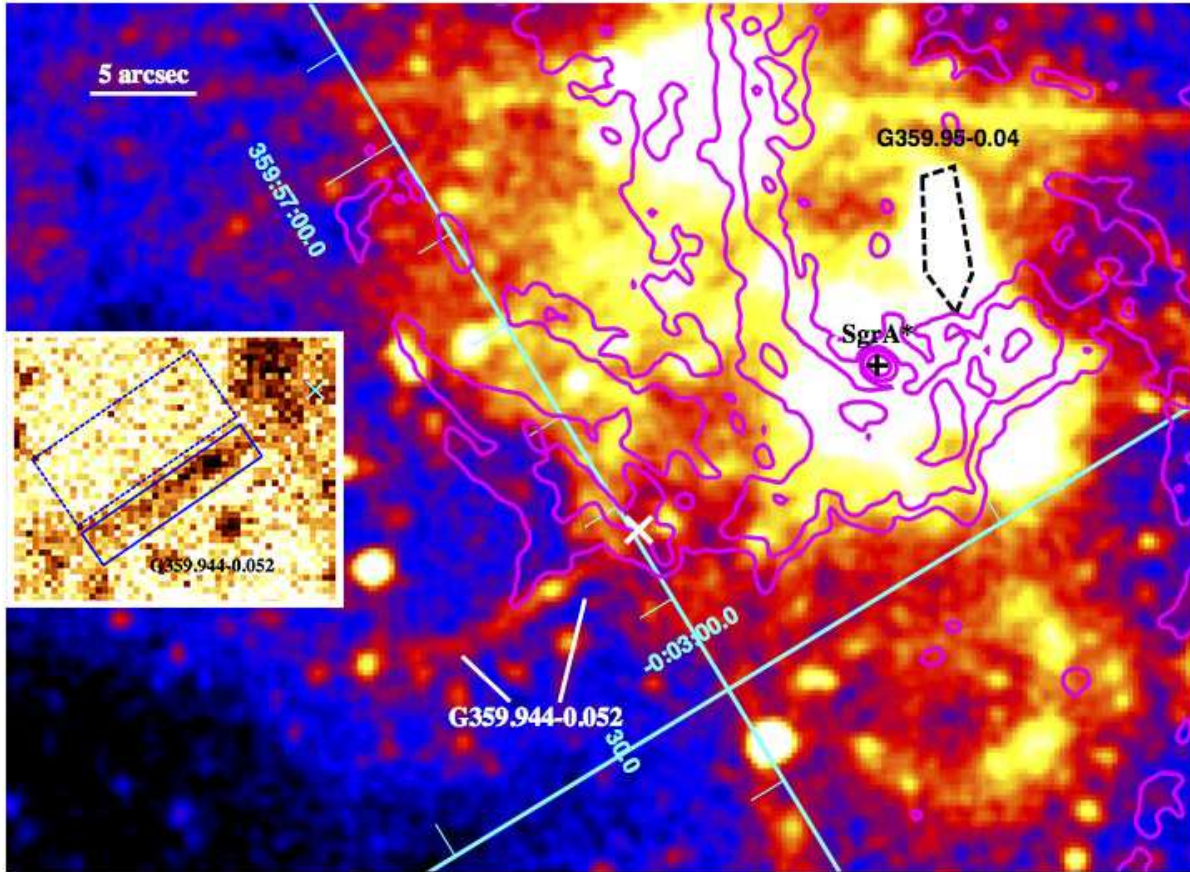


Fig. 1.— The 2–8 keV *Chandra* image of the linear filament G359.944-0.052, smoothed with a 2-pixel Gaussian kernel. The cyan grids denote Galactic coordinates. The ‘apex’ of the shock front (LMB13) is indicated with a white cross. The position of Sgr A* is marked with a ‘+’ sign. The color scale is chosen such that the filament is highlighted while the vicinity of Sgr A* is saturated. The magenta contours outline the structure of the mini-spiral as seen in VLA 8.4 GHz intensity map. We also mark the position of PWN G359.95-0.04 with a dashed polygon. The $7''.5 \times 1''.5$ solid box in the insert outlines the source extraction region, and the dashed box ($7''.5 \times 3''.0$) denotes the background region.

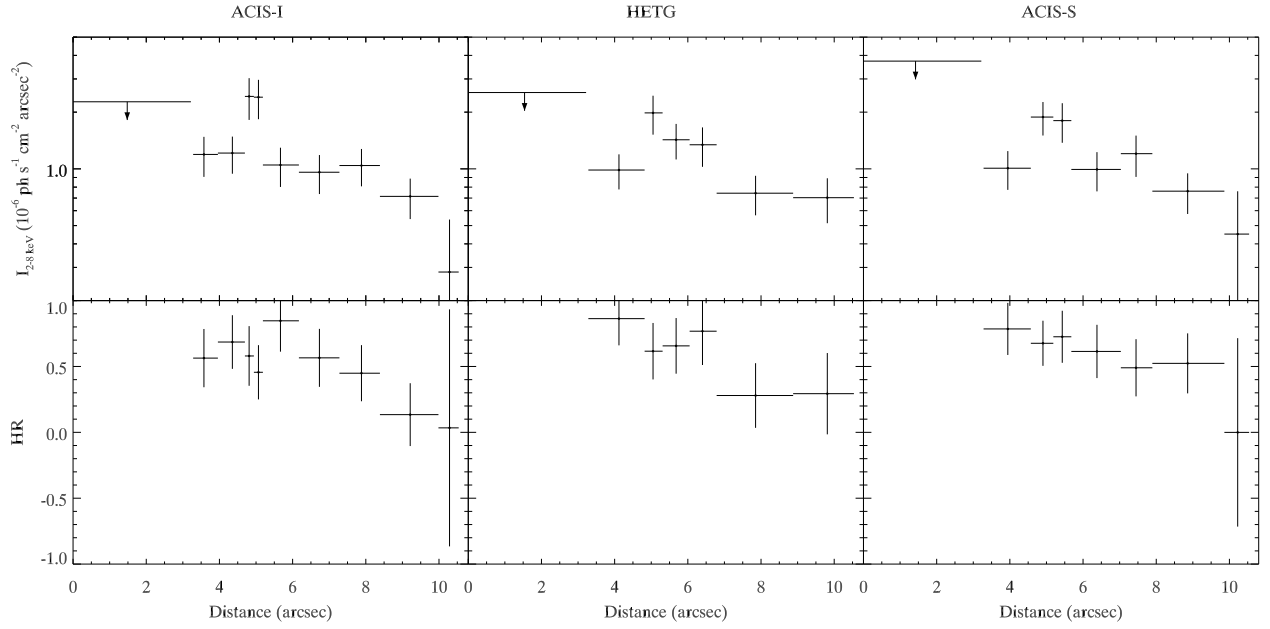


Fig. 2.— Spatial properties of G359.944-0.052. The first row shows the 2–8 keV intensity ($I_{2-8 \text{ keV}}$) profiles along the long-axis of the filament, averaged over a width of $1''.5$. The three panels display the data of ACIS-I, ACIS-S/HETG and ACIS-S/non-grating, respectively. The zero point is at the shock front on the Eastern Arm (marked by the ‘X’ sign in Figure 1). The first bin is subject to uncertain local background and thus is considered an upper limit. The rest of the profile is adaptively binned to achieve a minimum of 40 net counts and a S/N great than 4, except for the last bin. The second row shows the corresponding hardness ratio profiles, defined as $\text{HR} = (I_{4-8 \text{ keV}} - I_{2-4 \text{ keV}})/(I_{4-8 \text{ keV}} + I_{2-4 \text{ keV}})$.

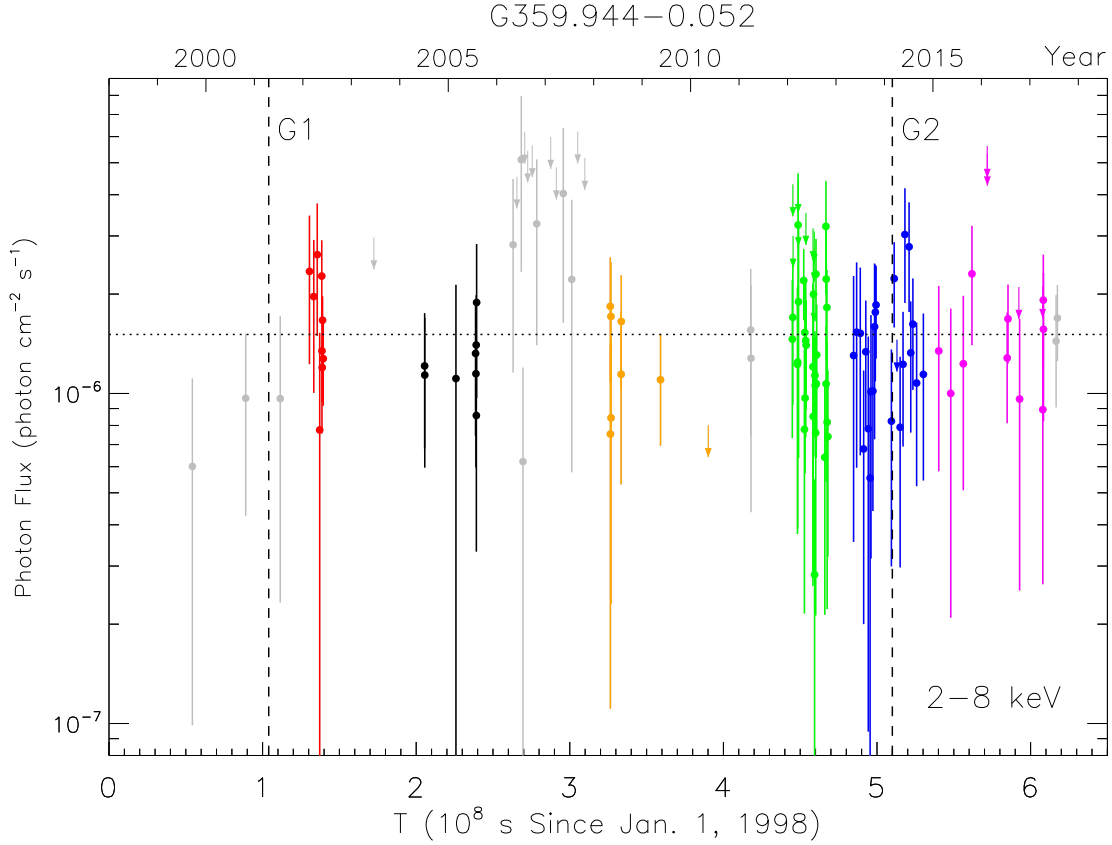


Fig. 3.— The 2–8 keV light curve of G359.944-0.052, combining the 122 *Chandra* observations. Arrows mark $3\text{-}\sigma$ upper limits for observations with limited net counts. Data points of different epochs are color-coded in the same way as in Figure 5b. Observations not included in the six epochs are marked with grey data points. The two dashed lines mark the estimated time of closest approach of G1 and G2 (Witzel et al. 2017). The mean photon flux is marked as a horizontal dotted line.

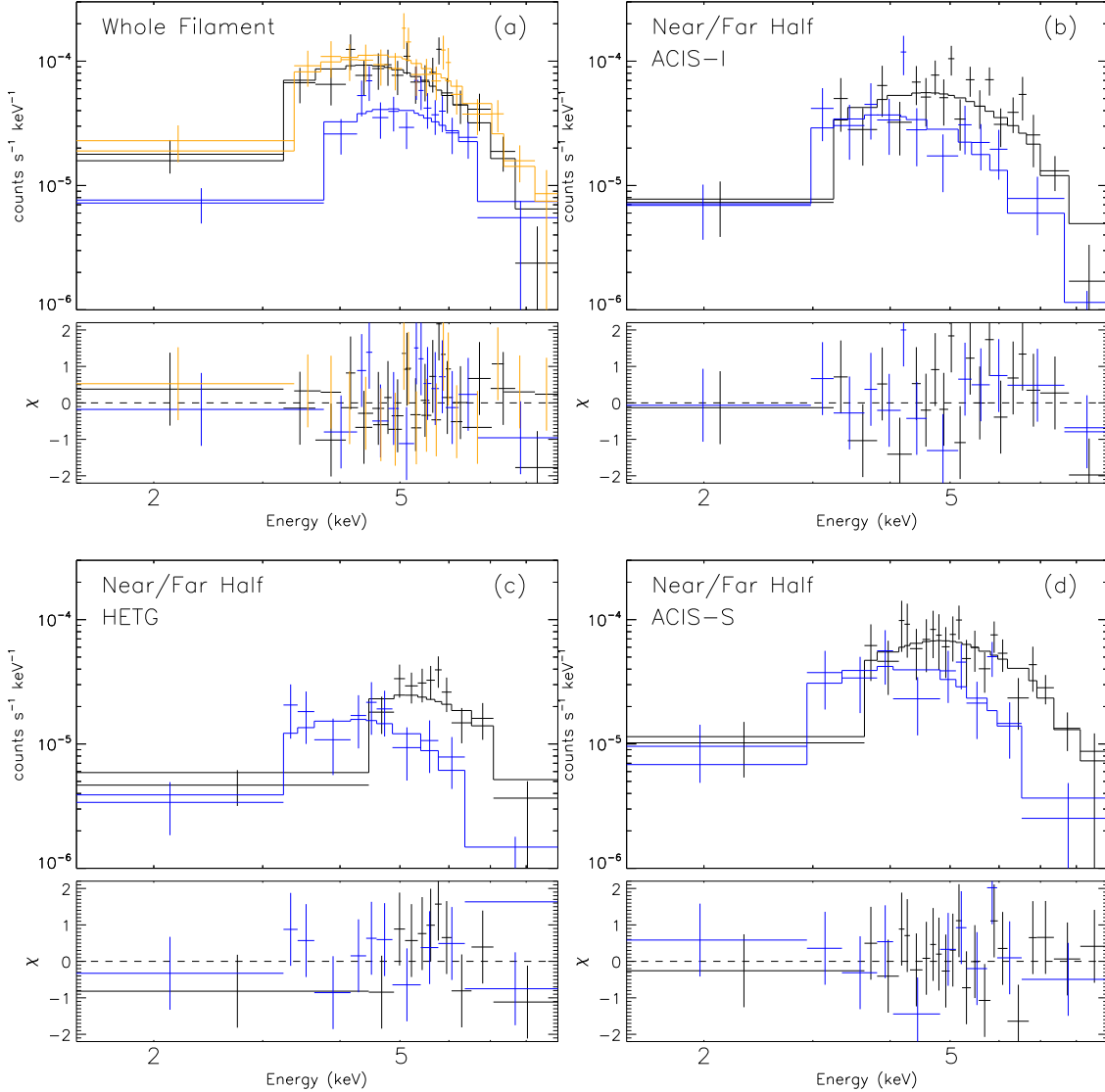


Fig. 4.— (a) The combined spectra of G359.944-0.052, adaptively binned to achieve S/N better than 3. The black/blue/orange data points represent the ACIS-I/HETG/ACIS-S spectrum; (b) ACIS-I spectra of the near-half (black) and far-half (blue) of G359.944-0.052. For these two regions, spectra extracted from HETG and ACIS-S are shown in (c) and (d). Also shown in all panels are the best-fit absorbed power-law models. The error bars represent 1- σ uncertainty.

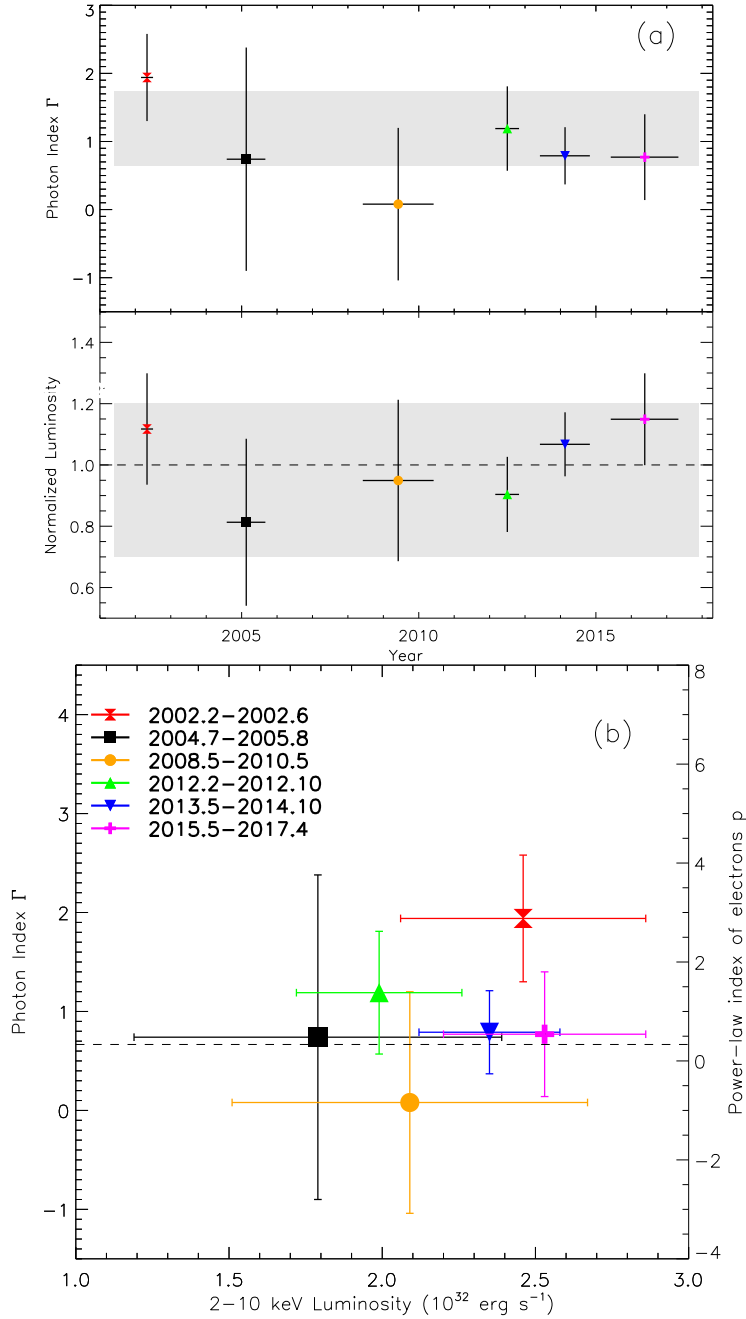


Fig. 5.— (a) Fitted photon-index and 2–10 keV luminosity (relative to the long-term mean) of the whole filament in six epochs. The grey strips indicate the range of pure statistical fluctuations inferred from simulated spectra. (b) The fitted power-law photon index (Γ ; $p = 2\Gamma - 1$) versus X-ray luminosity in the six epochs. The dashed line denotes the smallest possible photon-index predicted by the model of monoenergetic electrons (see Section 6). The error bars in both panels are of 90% uncertainty.

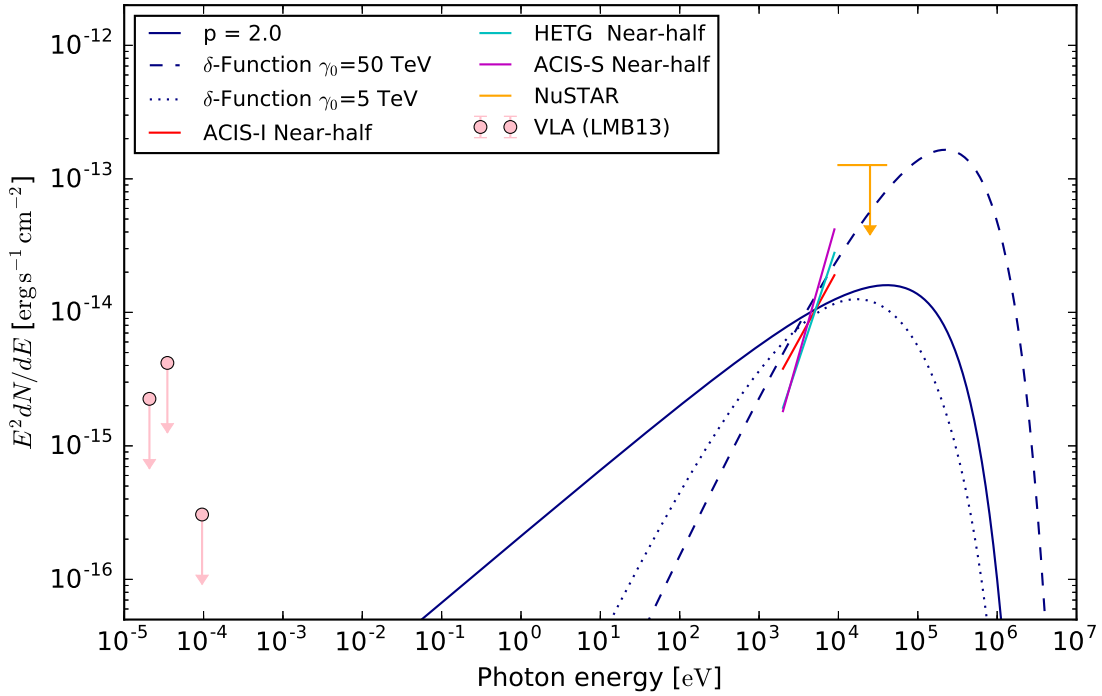


Fig. 6.— Steady-state synchrotron models characterizing the X-ray power-law spectrum, which also consistent with current $3\text{-}\sigma$ upper limits of radio data (1.33, 49.8 and 45.0 mJy at 23, 8.4, and 5.0 GHz, respectively; LMB13), denoted with pink arrows. The solid blue curve represents model with $p=2.0$, where p is the power-law slope of the electron energy distribution. The dashed and dotted curves show synchrotron emission models of monoenergetic electrons, following a δ -function distribution, with $\gamma_0=50$ TeV and $\gamma_0=5$ TeV respectively. The red, cyan and magenta line segment denotes the averaged near-half spectrum of ACIS-I, HETG and ACIS-S data respectively. The $3\text{-}\sigma$ upper limit given by *NuSTAR* in 10–40 keV band is marked with an orange arrow.

Table 1. *Chandra* Observation Log

ObsID	Start Time (UT)	Cleaned Exposure (ks)	Aim Point		Roll Angle (degree)
			R.A. (J2000)	Dec.	
ACIS-I					
242	1999-09-21 02:43:00	33.3	266.41399	-29.01271	268.7
15611	2000-10-26 19:08:03	35.5	266.41403	-29.01206	264.7
15612	2001-07-14 01:51:10	13.5	266.41549	-29.01238	280.7
2951	2002-02-19 14:27:32	12.4	266.41862	-29.00345	91.5
2952	2002-03-23 12:25:04	11.9	266.41891	-29.00353	88.2
2953	2002-04-19 10:59:43	11.6	266.41916	-29.00364	85.2
2954	2002-05-07 09:25:07	12.4	266.41938	-29.00374	82.1
2943	2002-05-22 23:19:42	36.8	266.41991	-29.00406	75.5
3663	2002-05-24 11:50:13	37.0	266.41993	-29.00407	75.5
3392	2002-05-25 15:16:03	164.7	266.41992	-29.00408	75.5
3393	2002-05-28 05:34:44	157.4	266.41992	-29.00407	75.5
3665	2002-06-03 01:24:37	89.3	266.41992	-29.00407	75.5
3549	2003-06-19 18:28:55	23.8	266.42095	-29.01052	346.8
4683	2004-07-05 22:33:11	49.5	266.41606	-29.01240	286.2
4684	2004-07-06 22:29:57	49.2	266.41597	-29.01239	285.4
6113	2005-02-27 06:26:04	4.9	266.41870	-29.00350	90.6
5950	2005-07-24 19:58:27	48.5	266.41519	-29.01225	276.7
5951	2005-07-27 19:08:16	42.3	266.41512	-29.01222	276.0
5952	2005-07-29 19:51:11	41.2	266.41508	-29.01222	275.5
5953	2005-07-30 19:38:31	40.2	266.41506	-29.01221	275.3
5954	2005-08-01 20:16:05	17.8	266.41503	-29.01218	274.9
6640	2006-05-03 22:26:26	5.1	266.41935	-29.00380	82.8
6641	2006-06-01 16:07:52	5.1	266.42019	-29.00437	69.7
6642	2006-07-04 11:01:35	5.1	266.41634	-29.01240	288.4
6363	2006-07-17 03:58:28	29.4	266.41542	-29.01231	279.5
6643	2006-07-30 14:30:26	5.0	266.41510	-29.01221	275.4
6644	2006-08-22 05:54:34	5.0	266.41485	-29.01205	271.7
6645	2006-09-25 13:50:35	4.5	266.41448	-29.01197	268.3
6646	2006-10-29 03:28:20	5.1	266.41425	-29.01181	264.4
7554	2007-02-11 06:16:55	4.8	266.41846	-29.00332	92.6
7555	2007-03-25 22:56:07	5.1	266.41414	-29.00002	88.0
7556	2007-05-17 01:05:03	5.0	266.41556	-28.99973	79.5
7557	2007-07-20 02:27:01	5.0	266.42069	-29.01498	278.4
7558	2007-09-02 20:19:41	5.0	266.41945	-29.01543	270.5
7559	2007-10-26 10:04:04	5.0	266.41868	-29.01564	264.8

Table 1—Continued

ObsID	Start Time (UT)	Cleaned Exposure (ks)	Aim Point		Roll Angle (degree)
			R.A. (J2000)	Dec.	
9169	2008-05-05 03:53:16	27.6	266.41522	-28.99981	81.7
9170	2008-05-06 03:00:30	26.8	266.41521	-28.99981	81.7
9171	2008-05-10 03:18:02	27.0	266.41522	-28.99980	81.7
9172	2008-05-11 03:36:46	27.4	266.41521	-28.99981	81.7
9174	2008-07-25 21:50:50	28.2	266.42039	-29.01521	276.4
9173	2008-07-26 21:20:49	27.8	266.42035	-29.01521	276.2
10556	2009-05-18 02:19:58	112.2	266.41566	-28.99975	79.0
11843	2010-05-13 02:12:34	78.6	266.41539	-28.99977	80.7
13016	2011-03-29 10:30:09	17.8	266.41431	-28.99996	87.6
13017	2011-03-31 10:30:09	17.8	266.41435	-28.99998	87.4

ACIS-S/HETG

13850	2012-02-06 00:38:33	59.3	266.41369	-29.00629	92.2
14392	2012-02-09 06:18:08	57.2	266.41369	-29.00628	92.2
14394	2012-02-10 03:17:24	17.5	266.41367	-29.00628	92.2
14393	2012-02-11 10:14:08	41.0	266.41369	-29.00629	92.2
13856	2012-03-15 08:46:28	38.9	266.41368	-29.00630	92.2
13857	2012-03-17 08:58:50	39.0	266.41369	-29.00628	92.2
13854	2012-03-20 10:13:19	22.8	266.41368	-29.00629	92.2
14413	2012-03-21 06:45:56	14.5	266.41367	-29.00630	92.2
13855	2012-03-22 11:25:56	19.8	266.41369	-29.00628	92.2
14414	2012-03-23 17:49:44	19.5	266.41366	-29.00629	92.2
13847	2012-04-30 16:17:58	151.7	266.41426	-29.00563	76.6
14427	2012-05-06 20:02:07	78.4	266.41426	-29.00563	76.4
13848	2012-05-09 12:03:55	96.2	266.41427	-29.00562	76.4
13849	2012-05-11 03:19:47	175.4	266.41427	-29.00563	76.4
13846	2012-05-16 10:42:22	51.2	266.41426	-29.00562	76.4
14438	2012-05-18 04:29:45	24.8	266.41427	-29.00561	76.4
13845	2012-05-19 10:43:37	133.5	266.41427	-29.00563	76.4
14460	2012-07-09 22:34:10	23.4	266.41991	-29.00884	282.3
13844	2012-07-10 23:12:04	19.8	266.41991	-29.00884	282.3
14461	2012-07-12 05:49:52	33.3	266.41991	-29.00885	282.3
13853	2012-07-14 00:38:24	72.7	266.41991	-29.00885	282.3
13841	2012-07-17 21:07:45	44.5	266.41992	-29.00885	282.3
14465	2012-07-18 23:24:45	33.9	266.41992	-29.00886	282.3
14466	2012-07-20 12:38:16	44.5	266.41991	-29.00884	282.3

Table 1—Continued

ObsID	Start Time (UT)	Cleaned Exposure (ks)	Aim Point		Roll Angle (degree)
			R.A. (J2000)	Dec.	
13842	2012-07-21 11:53:47	154.8	266.41991	-29.00885	282.3
13839	2012-07-24 07:04:06	135.8	266.41991	-29.00885	282.3
13840	2012-07-26 20:02:58	158.8	266.41991	-29.00885	282.3
14432	2012-07-30 12:57:08	73.3	266.41992	-29.00885	282.3
13838	2012-08-01 17:30:32	97.6	266.41991	-29.00885	282.3
13852	2012-08-04 02:38:43	153.9	266.41991	-29.00885	282.3
14439	2012-08-06 22:18:06	110.0	266.41960	-29.00940	270.7
14462	2012-10-06 16:33:00	131.4	266.41953	-29.00949	268.7
14463	2012-10-16 00:53:35	30.1	266.41954	-29.00948	268.7
13851	2012-10-16 18:49:52	104.7	266.41953	-29.00949	268.7
15568	2012-10-18 08:56:30	34.9	266.41954	-29.00950	268.7
13843	2012-10-22 16:01:55	117.2	266.41954	-29.00949	268.7
15570	2012-10-25 03:31:50	67.5	266.41953	-29.00949	268.7
14468	2012-10-29 23:43:14	143.2	266.41954	-29.00949	268.7
ACIS-S/Non-grating					
14702	2013-05-12 10:38:50	13.7	266.41484	-29.00586	80.7
14703	2013-06-04 08:45:16	16.8	266.41489	-29.00588	80.7
14946	2013-07-02 06:49:44	17.9	266.42241	-29.01387	290.9
15041	2013-07-27 01:27:17	44.5	266.42046	-29.01490	276.1
15042	2013-08-11 22:57:58	45.1	266.41706	-29.01561	253.7
14945	2013-08-31 10:12:46	17.3	266.42143	-29.01450	283.2
15043	2013-09-14 00:04:52	45.1	266.41946	-29.01524	269.3
14944	2013-09-20 07:02:56	18.2	266.42154	-29.01443	284.2
15044	2013-10-04 17:24:48	42.7	266.42103	-29.01465	280.2
14943	2013-10-17 15:41:05	18.2	266.42059	-29.01489	277.2
14704	2013-10-23 08:54:30	36.3	266.42049	-29.00932	274.2
15045	2013-10-28 14:31:14	45.1	266.41973	-29.01515	271.2
16508	2014-02-21 11:37:48	43.1	266.41232	-29.00086	100.2
16211	2014-03-14 10:18:27	41.7	266.41374	-29.00619	90.2
16212	2014-04-04 02:26:27	45.0	266.41386	-29.00605	87.0
16213	2014-04-28 02:45:05	44.1	266.41375	-29.00620	90.2
16214	2014-05-20 00:19:11	44.8	266.41410	-29.00577	80.2
16210	2014-06-03 02:59:23	17.0	266.41424	-29.00562	76.2
16597	2014-07-04 20:48:12	16.5	266.42002	-29.00855	287.9
16215	2014-07-16 22:43:52	41.5	266.42011	-29.00859	289.2

Table 1—Continued

ObsID	Start Time (UT)	Cleaned Exposure (ks)	Aim Point		Roll Angle (degree)
			R.A. (J2000)	Dec.	
16216	2014-08-02 03:31:41	42.7	266.41995	-29.00900	281.2
16217	2014-08-30 04:50:12	34.2	266.42005	-29.00878	285.2
16218	2014-10-20 08:22:28	36.0	266.41947	-29.00971	265.6
16963	2015-02-13 00:42:04	22.4	266.41256	-29.00375	92.3
16966	2015-05-14 08:46:51	22.4	266.41328	-29.00329	84.2
16965	2015-08-17 10:35:47	22.7	266.42079	-29.01191	272.4
16964	2015-10-21 06:04:57	22.6	266.42019	-29.01231	265.5
18055	2016-02-13 08:59:23	22.7	266.41391	-29.00775	92.3
18056	2016-02-14 14:46:01	21.8	266.41393	-29.00774	92.2
18731	2016-07-12 18:23:59	77.2	266.41952	-29.00767	281.3
18732	2016-07-18 12:01:38	75.4	266.41953	-29.00808	272.2
18057	2016-10-08 19:07:12	22.7	266.42092	-29.01167	267.2
18058	2016-10-14 10:47:43	22.4	266.41974	-29.00933	266.2
19726	2017-04-06 03:47:13	27.6	266.41337	-29.00658	86.7
19727	2017-04-07 04:57:18	27.5	266.41317	-29.00614	86.6
20041	2017-04-11 03:51:22	30.9	266.41261	-29.00489	86.1
20040	2017-04-12 05:18:22	27.2	266.41233	-29.00429	86.1
19703	2017-07-15 22:36:07	44.1	266.42159	-29.01160	270.2
19704	2017-07-25 22:57:27	77.8	266.42156	-29.01048	276.4

Note. — The 122 *Chandra* observations (45 with ACIS-I, 38 with ACIS-S/HETG and 39 with ACIS-S non-grating) of the GC. ObsIDs carried out with the same instrument are sorted by the observation time.

Table 2. Spectral Fit Results

Region (1)	Instrument (2)	$N_{\text{H},1}$ (3)	Γ_1 (4)	χ^2/dof (5)	L_{2-10} (6)	$N_{\text{H},2}$ (7)	Γ_2 (8)
All	ACIS-I	$17.6^{+5.14}_{-4.20}$	$1.40^{+0.50}_{-0.50}$	12.4/16	$1.96^{+0.25}_{-0.25}$	$13.1^{+6.75}_{-4.84}$	$1.62^{+0.50}_{-0.51}$
All	HETG	–	$1.18^{+0.62}_{-0.64}$	10.6/13	$1.99^{+0.37}_{-0.28}$	–	$1.40^{+0.62}_{-0.64}$
All	ACIS-S	–	$0.62^{+0.58}_{-0.60}$	9.7/17	$2.56^{+0.33}_{-0.32}$	–	$0.83^{+0.58}_{-0.61}$
Near	ACIS-I	–	$0.92^{+0.53}_{-0.53}$	20.6/18	$1.24^{+0.17}_{-0.18}$	–	$1.14^{+0.53}_{-0.52}$
Far	ACIS-I	–	$2.61^{+0.92}_{-0.95}$	8.7/11	$0.74^{+0.16}_{-0.17}$	–	$2.83^{+0.92}_{-0.95}$
Near	HETG	–	$0.20^{+0.66}_{-0.68}$	9.0/9	$1.38^{+0.24}_{-0.21}$	–	$0.43^{+0.66}_{-0.68}$
Far	HETG	–	$3.09^{+0.96}_{-1.03}$	4.1/9	$0.83^{+0.19}_{-0.20}$	–	$3.30^{+0.96}_{-1.03}$
Near	ACIS-S	–	$-0.10^{+0.63}_{-0.66}$	10.3/20	$1.89^{+0.26}_{-0.26}$	–	$0.11^{+0.63}_{-0.66}$
Far	ACIS-S	–	$1.92^{+1.09}_{-1.13}$	8.3/9	$0.74^{+0.03}_{-0.18}$	–	$2.13^{+1.09}_{-1.13}$

Note. — (1) Spectral extraction region: ‘All’ for the whole filament; ‘Near’ for the half of the filament closer to Sgr A*, defined by a $3.75'' \times 1.5''$ box; ‘Far’ for the far-half. (3)&(7) The fixed column density, in units of 10^{22} cm^{-2} . (4) The best-fit photon-index of the absorbed power-law model. (6) The unabsorbed 2-10 keV luminosity given a distance of 8 kpc, in units of $10^{32} \text{ erg s}^{-1}$. (8) The best-fit photon-index of the absorbed power-law model, with the foreground dust scattering considered. Quoted errors are at 90% confidence level.

Table 3. Spectral Fit Results of Various Epochs

No. (1)	Epoch (2)	Instrument (3)	Exposure (ks) (4)	Net Counts (5)	Γ (6)	χ^2/dof (7)	L_{2-10} (8)
1	2002.2-2002.6	ACIS-I	5.39×10^2	230	$1.94^{+0.64}_{-0.67}$	5.43/9	$2.46^{+0.40}_{-0.40}$
2	2004.7-2005.8	ACIS-I	3.05×10^2	90	$0.74^{+1.64}_{-1.57}$	5.02/5	$1.79^{+0.59}_{-0.60}$
3	2008.5-2010.5	ACIS-I	3.57×10^2	84	$0.08^{+1.12}_{-1.23}$	1.32/4	$2.09^{+0.58}_{-0.58}$
4	2012.2-2012.10	HETG	2.83×10^3	381	$1.19^{+0.62}_{-0.64}$	9.57/13	$1.99^{+0.27}_{-0.28}$
5	2013.5-2014.10	ACIS-S	7.68×10^2	290	$0.79^{+0.42}_{-0.43}$	11.50/17	$2.35^{+0.23}_{-0.24}$
6	2015.5-2017.4	ACIS-S	5.45×10^2	217	$0.77^{+0.63}_{-0.67}$	8.32/7	$2.53^{+0.33}_{-0.32}$

Note. — (5) Net counts in the 1–9 keV band. (6) The best-fit photon-index of the absorbed power-law model. (8) The intrinsic 2-10 keV luminosity, given a distance of 8kpc, in units of 10^{32} erg s^{-1} . Quoted errors are at 90% confidence level.

Appendix

For ease of reference, Table A1 lists the 2–8 keV photon flux (or 3σ upper limit in the case of non-detection) of G359.944 in each observation, same as presented in Figure 3.

Table A1. 2–8 keV photon flux of G359.944 in individual observations

ObsID (1)	C_{tot} (2)	C_{net} (3)	F_{2-8} (4)
ACIS-I			
242	21	5.21	$0.60^{+1.11}_{-0.10}$
15611	25	9.68	$0.97^{+1.52}_{-0.43}$
15612	8	3.69	$0.96^{+1.72}_{-0.23}$
2951	13	8.21	$2.34^{+3.46}_{-1.23}$
2952	9	6.61	$1.97^{+2.92}_{-1.00}$
2953	12	8.65	$2.63^{+3.76}_{-1.49}$
2954	8	2.74	$0.78^{+1.53}_{-0.05}$
2943	38	23.64	$2.27^{+2.91}_{-1.63}$
3663	31	14.25	$1.35^{+1.94}_{-0.76}$
3392	115	56.61	$1.20^{+1.45}_{-0.94}$
3393	147	75.21	$1.67^{+1.97}_{-1.37}$
3665	66	32.50	$1.27^{+1.63}_{-0.92}$
3549	10	1.86	< 2.97
4683	36	13.50	$1.21^{+1.75}_{-0.68}$
4684	37	12.11	$1.14^{+1.69}_{-0.60}$
6113	2	1.52	$1.11^{+2.13}_{-0.08}$
5950	42	14.24	$1.32^{+1.91}_{-0.74}$
5951	31	11.38	$1.15^{+1.72}_{-0.60}$
5952	33	14.81	$1.40^{+1.98}_{-0.83}$
5953	28	7.90	$0.86^{+1.40}_{-0.33}$
5954	16	8.34	$1.89^{+2.84}_{-0.97}$
6640	5	4.04	$2.82^{+4.47}_{-1.16}$
6641	2	0.00	< 4.54
6642	8	5.13	$5.11^{+7.97}_{-2.34}$
6363	22	3.33	$0.62^{+1.20}_{-0.06}$
6643	3	0.13	< 6.20
6644	3	0.00	< 5.44
6645	2	0.09	< 5.64
6646	6	4.56	$3.27^{+5.12}_{-1.40}$
7554	4	0.00	< 5.98
7555	1	0.04	< 4.84
7556	6	4.56	$4.03^{+6.38}_{-1.64}$
7557	5	3.09	$2.22^{+3.86}_{-0.58}$
7558	3	1.56	< 6.22
7559	2	0.56	< 5.17
9169	19	12.30	$1.84^{+2.59}_{-1.08}$

Table A1—Continued

ObsID (1)	C_{tot} (2)	C_{net} (3)	F_{2-8} (4)
9170	17	5.51	$0.75^{+1.40}_{-0.11}$
9171	18	10.82	$1.71^{+2.50}_{-0.93}$
9172	14	5.86	$0.84^{+1.47}_{-0.23}$
9174	20	8.99	$1.14^{+1.77}_{-0.53}$
9173	20	12.82	$1.65^{+2.28}_{-1.03}$
10556	62	27.06	$1.10^{+1.51}_{-0.69}$
11843	29	0.00	< 0.80
13016	13	7.74	$1.56^{+2.38}_{-0.74}$
13017	13	6.30	$1.28^{+2.13}_{-0.44}$

ACIS-S/HETG

13850	19	9.43	$1.46^{+2.20}_{-0.73}$
14392	21	10.95	$1.70^{+2.49}_{-0.92}$
14394	4	0.00	< 4.30
14393	11	1.91	< 3.00
13856	13	5.34	$1.23^{+2.09}_{-0.37}$
13857	13	5.34	$1.24^{+2.13}_{-0.39}$
13854	11	8.13	$3.24^{+4.64}_{-1.81}$
14413	2	0.09	< 4.40
13855	4	0.00	< 3.49
14414	7	4.13	$1.90^{+3.18}_{-0.64}$
13847	66	36.80	$2.20^{+2.74}_{-1.67}$
14427	24	6.77	$0.78^{+1.36}_{-0.22}$
13848	36	16.38	$1.53^{+2.17}_{-0.91}$
13849	47	18.76	$0.97^{+1.37}_{-0.57}$
13846	16	8.82	$1.45^{+2.17}_{-0.74}$
14438	5	1.17	< 3.52
13845	45	20.59	$1.40^{+1.92}_{-0.89}$
14460	6	3.13	$1.21^{+2.15}_{-0.26}$
13844	2	0.00	< 3.16
14461	9	4.69	$0.85^{+1.43}_{-0.28}$
13853	25	15.91	$2.00^{+2.68}_{-1.32}$
13841	8	0.00	< 2.06
14465	10	1.86	< 2.72
14466	13	2.95	< 3.10
13842	37	5.89	$0.28^{+0.55}_{-0.02}$
13839	47	21.63	$1.13^{+1.54}_{-0.74}$

Table A1—Continued

ObsID (1)	C_{tot} (2)	C_{net} (3)	F_{2-8} (4)
13840	43	18.59	$1.06^{+1.48}_{-0.64}$
14432	19	6.08	$0.76^{+1.32}_{-0.21}$
13838	40	24.68	$2.30^{+2.94}_{-1.66}$
13852	43	18.11	$1.07^{+1.51}_{-0.64}$
14439	35	15.86	$1.31^{+1.86}_{-0.76}$
14462	36	9.20	$0.64^{+1.08}_{-0.21}$
14463	14	10.65	$3.21^{+4.40}_{-2.00}$
13851	31	12.33	$1.07^{+1.61}_{-0.54}$
15568	12	8.65	$2.22^{+3.17}_{-1.26}$
13843	42	23.81	$1.82^{+2.37}_{-1.28}$
15570	20	6.12	$0.82^{+1.44}_{-0.22}$
14468	38	11.68	$0.74^{+1.17}_{-0.32}$

ACIS-S/Non-grating

14702	13	5.34	$1.30^{+2.27}_{-0.35}$
14703	19	7.51	$1.53^{+2.49}_{-0.60}$
14946	18	7.95	$1.52^{+2.41}_{-0.65}$
15041	38	8.80	$0.68^{+1.17}_{-0.20}$
15042	44	17.68	$1.34^{+1.91}_{-0.78}$
14945	14	3.95	$0.78^{+1.49}_{-0.09}$
15043	47	7.27	$0.55^{+1.04}_{-0.07}$
14944	13	5.34	$1.01^{+1.73}_{-0.32}$
15044	43	12.85	$1.02^{+1.60}_{-0.44}$
14943	18	8.43	$1.59^{+2.48}_{-0.73}$
14704	41	18.50	$1.76^{+2.46}_{-1.09}$
15045	47	24.50	$1.85^{+2.43}_{-1.28}$
16508	35	9.63	$0.82^{+1.36}_{-0.30}$
16211	50	27.03	$2.23^{+2.87}_{-1.58}$
16212	29	0.76	< 1.46
16213	35	11.07	$0.79^{+1.29}_{-0.30}$
16214	39	16.03	$1.23^{+1.77}_{-0.69}$
16210	26	14.99	$3.03^{+4.18}_{-1.88}$
16597	20	13.30	$2.78^{+3.79}_{-1.76}$
16215	37	15.94	$1.33^{+1.90}_{-0.76}$
16216	44	20.07	$1.62^{+2.23}_{-1.02}$
16217	25	10.64	$1.08^{+1.64}_{-0.52}$
16218	29	12.25	$1.14^{+1.75}_{-0.54}$

Table A1—Continued

ObsID	C_{tot}	C_{net}	F_{2-8}
(1)	(2)	(3)	(4)
16963	18	8.43	$1.34^{+2.12}_{-0.58}$
16966	21	6.64	$1.00^{+1.81}_{-0.21}$
16965	20	8.03	$1.23^{+1.98}_{-0.51}$
16964	29	15.12	$2.30^{+3.22}_{-1.40}$
18055	100	5.71	< 5.62
18056	98	1.80	< 5.33
18731	85	28.52	$1.28^{+1.76}_{-0.81}$
18732	77	36.80	$1.68^{+2.14}_{-1.23}$
18057	12	1.47	< 2.10
18058	20	6.60	$0.96^{+1.68}_{-0.25}$
19726	17	3.12	< 2.11
19727	22	7.64	$0.89^{+1.54}_{-0.26}$
20041	28	16.51	$1.92^{+2.63}_{-1.21}$
20040	23	11.99	$1.56^{+2.32}_{-0.82}$
19703	38	18.38	$1.44^{+1.99}_{-0.91}$
19704	78	37.80	$1.69^{+2.13}_{-1.25}$

Note. — (1) Observation ID; (2)-(3) 2–8 keV total counts and net counts of G359.944. (4) The 2–8 keV photon flux, in units of 10^{-6} erg s $^{-1}$ cm $^{-2}$. For the observations with sufficient net counts, the quoted errors are at $1\text{-}\sigma$ confidence level. For other observations with limited net counts, $3\text{-}\sigma$ upper limits are given (arrows in Figure 3).